RSC Advances

ROYAL SOCIETY OF CHEMISTRY

PAPER

View Article Online
View Journal | View Issue

Check for updates

Cite this: *RSC Adv.*, 2025, **15**, 39696

Two-dimensional TaS_2 as a contact material for MXene Sc_2CF_2 semiconductors: a first-principles study

Tuan V. Vu,[ab] Phan T. T. Huyen,[c] Nguyen N. Hieu,*[de] Huynh V. Phuc*[f] and Chuong V. Nguyen[g]

Received 25th July 2025
Accepted 11th October 2025

DOI: 10.1039/d5ra05385d

rsc.li/rsc-advances

Metal–semiconductor heterojunctions are fundamental to modern electronics, serving as the key interface for charge transport and enabling diverse functionalities in electronic and optoelectronic devices. In this work, we computationally design the electrical contact architecture by vertically integrating two-dimensional TaS_2 and Sc_2CF_2 materials using first-principles predictions. The TaS_2/Sc_2CF_2 heterostructure is predicted to be energetically and thermally stable at room temperature and characterized by weak van der Waals interactions. Additionally, the integration of TaS_2 with Sc_2CF_2 enhances the mechanical rigidity of the heterostructure. More interestingly, the TaS_2/Sc_2CF_2 heterostructure forms a Schottky contact with an electron barrier of 0.36 eV. Furthermore, it exhibits remarkable tunability in electronic properties and contact behavior under an applied electric field. Specifically, the electric field induces a transition from Schottky to ohmic contact, as well as a conversion from n-type to p-type Schottky contact. This tunability signifies a barrier-free charge injection process, making the TaS_2/Sc_2CF_2 heterostructure a promising candidate for next-generation electronic and optoelectronic devices.

1 Introduction

Two-dimensional (2D) materials have revolutionized the field of electronic devices due to their unique structures and extraordinary properties.[1,2] Since the discovery of graphene,[3] extensive research has led to the exploration of various 2D material families, each offering distinct advantages. Hexagonal boron nitride (*h*-BN), a wide-bandgap insulator,[4] serves as an ideal dielectric substrate due to its atomically smooth surface and minimal charge trapping effects.[5,6] Transition metal dichalcogenides (TMDCs),[7] with their tunable band gaps[8,9] and high carrier mobility,[10] have enabled advancements in optoelectronic devices[11] and low-power transistors.[12,13] Meanwhile, MXenes,[14] a versatile class of layered transition metal carbides and nitrides, exhibit mechanically robust,[15,16] broadening their potential for energy storage and catalysis.[17,18] These diverse functionalities pave the way for innovative heterostructures, where synergistic interactions between 2D materials can be harnessed to tailor electronic and interfacial properties for next-generation applications.[19,20]

Among the diverse family of TMDCs, tantalum disulfide (TaS_2) stands out due to its intrinsic metallic nature and intriguing electronic properties.[21] Unlike semiconducting TMDCs, TaS_2 exhibits a highly conductive behavior attributed to its layered structure and strong electron correlation effects.[22] Its metallic state enables efficient charge transport, making it a promising candidate for applications in interconnects, low-resistance contacts, and electronic devices requiring high conductivity.[23] Moreover, the integration of metallic TaS_2 with semiconducting 2D materials opens new avenues for designing high-performance heterostructures with tailored electronic and interfacial properties.[24–26]

Similar to metallic TaS_2, most MXenes exhibit intrinsic metallic behavior.[27] However, Sc_2CF_2 stand out as rare exceptions, displaying semiconducting characteristics due to their unique surface terminations and structural modifications.[28] Owing to these intriguing properties, Janus MXenes have recently been predicted to be promising candidates for applications in nanoelectronics, optoelectronics, and energy conversion devices, further broadening the potential of Sc-based MXenes.[29–31] In particular, Sc_2CF_2, with its well-defined

---

[a] *Laboratory for Computational Physics, Institute for Computational Science and Artificial Intelligence, Van Lang University, Ho Chi Minh City, Vietnam. E-mail: tuan.vu@vlu.edu.vn*

[b] *Faculty of Mechanical, Electrical, and Computer Engineering, Van Lang School of Technology, Van Lang University, Ho Chi Minh City, Vietnam*

[c] *Hue FPT School, Hue, Vietnam*

[d] *Institute of Research and Development, Duy Tan University, Da Nang 550000, Vietnam. E-mail: hieunn@duytan.edu.vn*

[e] *Faculty of Natural Sciences, Duy Tan University, Da Nang 550000, Vietnam*

[f] *Division of Physics, School of Education, Dong Thap University, Dong Thap 870000, Vietnam. E-mail: hvphuc@dthu.edu.vn*

[g] *Department of Materials Science and Engineering, Le Quy Don Technical University, Hanoi 100000, Vietnam*

band gap[32] and tunbale electronic properties,[33,34] emerges as an effective semiconducting channel for integration with other 2D materials.[29,35–38] Therefore, in this work, we employ first-principles calculations to design and analyze the electrical contact between metallic TaS_2 and semiconducting Sc_2CF_2, aiming to establish a high-performance metal–semiconductor heterostructure with tailored electronic properties. Our results reveal that the TaS_2/Sc_2CF_2 heterostructure naturally forms a p-type Schottky contact with a relatively low barrier height of 0.36 eV. More importantly, this contact behavior can be effectively tuned by an external electric field, which induces a transition between n-type and p-type Schottky contacts. It should be noted that the Schottky junction plays a vital role in modern electronics and spintronics owing to its ability to control carrier injection and band alignment at metal–semiconductor interfaces, which directly determines the performance of transistors, photodetectors, and nanoelectronic devices. These results provide valuable insights into the interfacial physics of the TaS_2/Sc_2CF_2 heterostructure, paving the way for the design of next-generation electronic devices, such as field-effect transistors and photodetectors with enhanced efficiency and functionality based on the TaS_2/Sc_2CF_2 heterostructure.

2 Computational methods

To investigate the electronic properties and contact characteristics of the TaS_2/Sc_2CF_2 heterostructure, we performed first-principles calculations based on density functional theory (DFT) as implemented in the Vienna *Ab initio* Simulation Package (VASP).[39] The exchange–correlation interactions were treated using the generalized gradient approximation (GGA) in the Perdew–Burke–Ernzerhof (PBE) functional.[40] Additionally, van der Waals (vdW) interactions were accounted for by employing the DFT-D3 correction method[41] to ensure accurate representation of interlayer interactions. The plane-wave basis set was used with a kinetic energy cutoff of 510 eV to ensure sufficient convergence in electronic structure calculations. A 12 × 12 × 1 Monkhorst–Pack *k*-point mesh[42] was employed for Brillouin zone sampling. To model the TaS_2/Sc_2CF_2 heterostructure, a vacuum layer of 25 Å was introduced to eliminate spurious interactions between periodic images. The atomic structures were fully optimized until the total energy was converged to within 10^{-8} eV and the residual force on each atom was smaller than 0.01 eV $Å^{-1}$. To evaluate the structural stability of the TaS_2/Sc_2CF_2 heterostructure, both *ab initio* molecular dynamics (AIMD)[43] simulations and phonon dispersion calculations were carried out. The AIMD simulations were performed within the canonical (NVT)[44] ensemble using a Nosé–Hoover thermostat at 300 K for a total simulation time of 9 ps with a time step of 1 fs. In addition, the phonon spectra were calculated using density functional perturbation theory (DFPT).[45]

3 Results and discussion

The TaS_2/Sc_2CF_2 heterostructure is designed *via* vertical integration of a (1 × 1) unit cell of TaS_2 and a (1 × 1) unit cell of Sc_2CF_2 monolayer. This design is facilitated by their minimal lattice mismatch, with TaS_2 exhibiting a lattice constant of 3.31 Å and Sc_2CF_2 having a slightly larger value of 3.34 Å. The atomic structures of the TaS_2/Sc_2CF_2 heterostructure are illustrated in Fig. 1. Due to the hexagonal symmetry of the TaS_2 and Sc_2CF_2 monolayers, many of these possible arrangements are symmetry-equivalent or can be obtained by simple in-plane translations of the constituent monolayers. Therefore, we focused on four representative four stacking arrangements, which capture the physically distinct registries, namely on-top, hollow, and bridge-like configurations, as illustrated in Fig. 1. The interlayer spacing *d* between the lowest sulfur (S) layer and the topmost fluorine (F) layer has been calculated. Among the configurations, the TS2 stacking exhibits the shortest interlayer spacing at 2.72 Å, while the TS1 stacking shows the largest spacing of 3.29 Å. It is evident that the obtained interlayer spacing *d* remains larger than the sum of the covalent bond lengths of fluorine (0.57 Å) and sulfur (1.05 Å) atoms. This observation suggests that the TaS_2/Sc_2CF_2 heterostructure is primarily stabilized by weak van der Waals (vdW) interactions rather than strong chemical bonding. Furthermore, these values of *d* are also comparable with those obtained in other vdW typical heterostructures,[35,37,38,46] further confirming the weak vdW interactions in the TaS_2/Sc_2CF_2 heterostructure. Furthermore, the binding energy is also evaluated to quantify the stability of the TaS_2/Sc_2CF_2 heterostructure. The binding energy per unit cell (E_b) is calculated using the formula:

$$E_b = \frac{E_H - (E_{TaS_2} + E_{Sc_2CF_2})}{A} \quad (1)$$

where E_H represents the total energy of the TaS_2/Sc_2CF_2 system, E_{TaS_2} and $E_{Sc_2CF_2}$ correspond to the individual total energies of the monolayers, and *A* denotes the area of the heterostructure. A negative binding energy indicates an energetically favorable interaction, confirming the structural stability driven by vdW forces. Among the stacking configurations, TS_2 exhibits the lowest binding energy of Eb = −18.73 meV Å−2, indicating the most stable arrangement. In contrast, the TS_1 stacking presents the highest binding energy of Eb = −11.45 meV Å−2. These results highlight the TS_2 stacking as the most energetically favorable configuration for the TaS_2/Sc_2CF_2 heterostructure. Additionally, the electron localization function (ELF) for the TS2 stacking configuration is visualized to describe the bonding nature of the TaS_2/Sc_2CF_2 heterostructure, as depicted in Fig. S1 of the SI. It is obvious that the high ELF values (close to 1.0) are mainly localized around the S and F atoms, indicating strong covalent bonding within the TaS_2 and Sc_2CF_2 layers. In contrast, the interfacial region between TaS_2 and Sc_2CF_2 layers exhibits very low ELF values (close to 0.0), confirming that the interaction across the interface is weak and dominated by vdW forces. To gain deeper insights into the stability and electronic behavior of the TS_2 stacking, we extend our analysis to its mechanical properties, band structures, and charge redistribution.

The projected band structures of the TaS_2/Sc_2CF_2 heterostructure are illustrated in Fig. 2. It is evident that the TaS_2/Sc_2CF_2 heterostructure exhibits metallic behavior, characterized

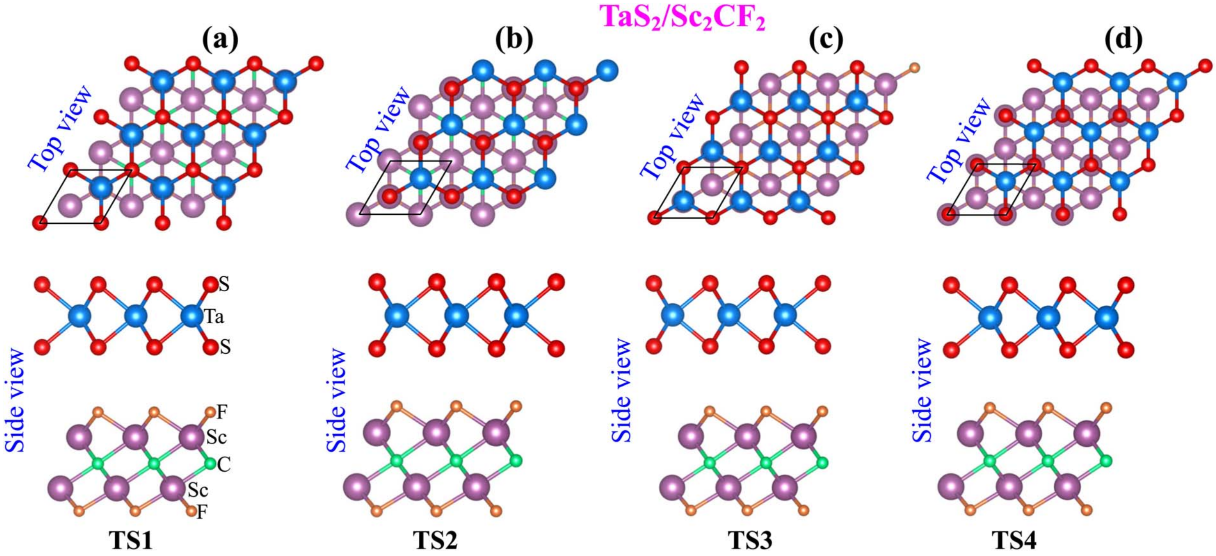

Fig. 1 Optimized atomic structures of the TaS_2/Sc_2CF_2 heterostructure for different stacking arrangements of (a) TS1, (b) TS2, (c) TS3 and (d) TS4. Red and blue balls represent the S and Ta atoms, respectively. While, orange, violet and green balls stand for the F, Sc and C atoms, respectively.

by crossing bands at the Fermi level. Additionally, the band structures of the TaS_2/Sc_2CF_2 heterostructure, irrespective of the stacking arrangement, closely resemble the sum of those of the individual monolayers, as illustrated in Fig. S2. Besides, it is evident that the band crossing at the Fermi level of the heterostructure is primarily contributed by the Ta atoms from the TaS_2 layer. On the other hand, the CB of the Sc_2CF_2 layer originates mainly from the Sc atom, while its VB is due to the orbital hybridization between C and F atoms, as illustrated in Fig. S3. This band alignment mechanism arises due to the weak vdW interactions between the TaS_2 and Sc_2CF_2 layers, preserving the electronic characteristics of the constituent materials. Furthermore, the metal–semiconductor TaS_2/Sc_2CF_2 heterostructure is primarily characterized by the formation of either Schottky or ohmic contact. As illustrated in Fig. 2, the metallic TaS_2 layer exhibits band crossings at the Fermi level, while the Fermi level is positioned between the conduction and valence band edges of the Sc_2CF_2 layer. This band alignment suggests the formation of a Schottky contact at the TaS_2/Sc_2CF_2 heterostructure. The Schottky barriers of the TaS_2/Sc_2CF_2 heterostructure are defined as follows:

$$\Phi_e = E_c - E_F,\ \Phi_h = E_F - E_v \tag{2}$$

where Φ_e and Φ_h represent the Schottky barrier heights for electrons and holes, respectively. E_c and E_v denote the conduction and valence band edges of the Sc_2CF_2 semiconductor, while E_F is the Fermi level of the heterostructure. The calculated barrier heights provide insights into charge carrier transport mechanisms at the interface. Our results reveal that the TS2 configuration has the narrowest Φ_h of 0.36 eV and highest Φ_e of 0.71 eV. While the TS1 configuration has the highest Φ_h of 0.41 eV and narrowest Φ_e of 0.65 eV. A lower Schottky barrier facilitates electron injection and enhances conductivity, whereas a higher barrier height restricts charge flow, influencing the electronic properties of the heterostructure. These values of the Schottky barriers are comparable with those in other 2D vdW metal–semiconductor

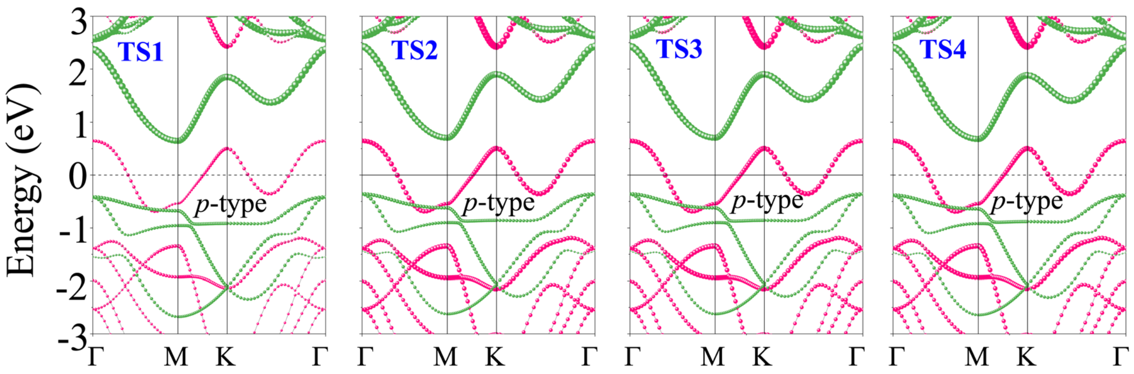

Fig. 2 Projected band structures of the TaS_2/Sc_2CF_2 heterostructure. Purple and green lines represent the projections of the band structures of TaS_2 and Sc_2CF_2 layers, respectively. The Fermi level is set to be zero.

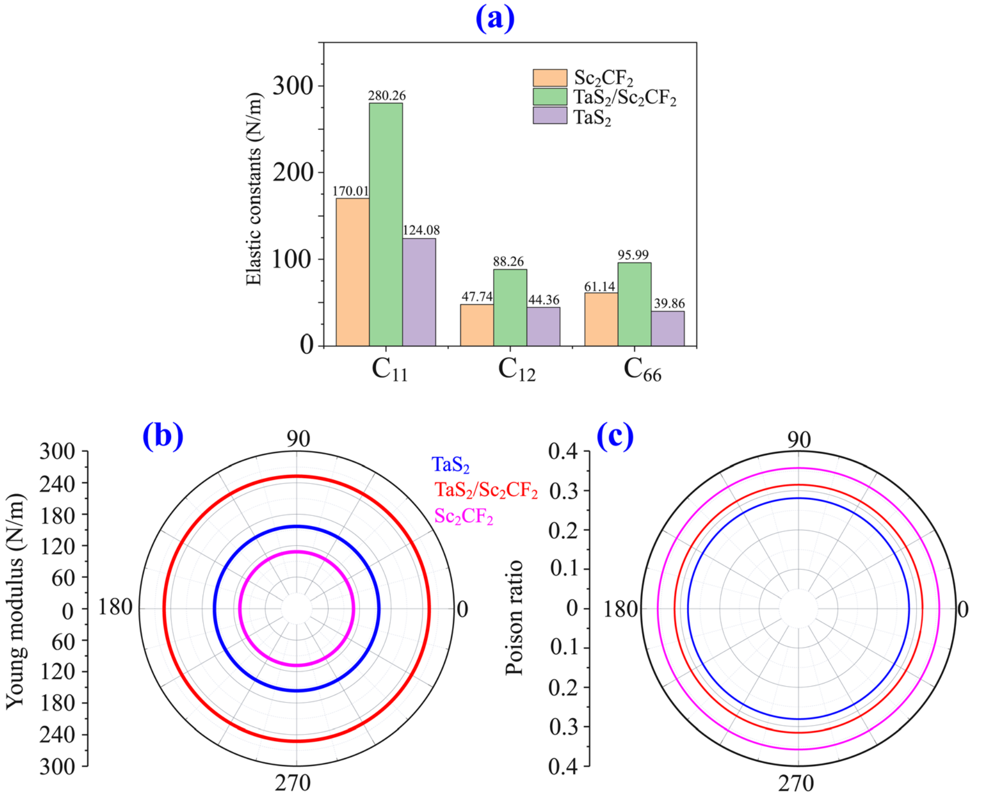

Fig. 3 (a) Calculated elastic constants (b) Young modulus and (c) Poison ratio of the TaS_2/Sc_2CF_2 heterostructure and the constituent monolayers.

heterostructures.[47,48] In the TaS_2/Sc_2CF_2 heterostructure, the barriers for holes Φ_h is consistently lower than that for electrons (Φ_e), indicating the formation of an p-type Schottky contact. Furthermore, to validate the accuracy of the calculated method, we provide the HSE06 projected band structure of the TaS_2/Sc_2CF_2 heterostruture for the TS2 stacking configuration, as illustrated in Fig. S3 of the SI. The Φ_h and Φ_e are obtained to be 0.38 and 1.48 eV, respectively, confirming the formation of the p-type Schottky contact. In addition, since the difference between the HSE06 and PBE results is relatively small, we have opted to employ the PBE method for the remaining calculations to ensure computational efficiency. This type of contact is advantageous for efficient hole transport across the interface, making the heterostructure highly promising for electronic and optoelectronic applications, such as field-effect transistors (FETs) and photodetectors.

In order to examine the mechanical stability, we performed elastic constant calculations using the energy-strain technique through the harmonic approximation, expressed as:[49]

$$\Delta E = \frac{V_0}{2}\sum_{i=1}^{6}\sum_{j=1}^{6} C_{i,j} e_i e_j \tag{3}$$

where ΔE and V_0 represent the energy and volume differences between the strained and unstrained unit cells, respectively, while the strain vector components are denoted as e_i and e_j. The TaS_2/Sc_2CF_2 heterostructure possesses four independent elastic constants: C_{11}, C_{22}, C_{12}, and C_{66}. Specifically, C_{11} and C_{22} denote in-plane stiffness against uniaxial strain along the x and y direction, respectively, while C_{12} describes the coupling between strain along the x direction and the induced stress along the y direction. It determines how deformation in the x direction induces stress in the y direction. Because of the hexagonal symmetry, $C_{11} = C_{22}$, which ensures that the in-plane Young's modulus and Poison ration are isotropic. The shear constant C_{66} characterizes the resistance to in-plane shear deformation and, for hexagonal symmetry, is not independent but can be expressed as $C_{66} = (C_{11} - C_{12})/2$. These values, along with those of the TaS_2 and Sc_2CF_2 monolayers, are presented in Fig. 3(a). Notably, the TaS_2/Sc_2CF_2 heterostructure exhibits larger elastic constants C_{ij} compared to its constituent monolayers, indicating enhanced mechanical rigidity. Furthermore, the obtained elastic constants satisfy the Born-Huang stability criteria ($C_{11} > C_{12}$ and $C_{66} > 0$), confirming the mechanical stability of the heterostructure. This improvement enables the material to better withstand external mechanical stress and deformation while maintaining its structural integrity. To further assess the mechanical properties of the TaS_2/Sc_2CF_2 heterostructure, we evaluate Young's modulus (Y) and Poisson's ratio (ν), which provide insights into the material's stiffness and deformation characteristics.[50]

$$Y(\theta) = \frac{C_{11}C_{12} - {C_{11}}^2}{C_{11}\ \sin^4(\theta) + C_{22}\ \cos^4(\theta) + \chi\ \sin^2(\theta)\cos^2(\theta)}, \tag{4}$$

$$\nu(\theta)=\frac{\gamma\ \sin^2(\theta)\cos^2(\theta)-C_{12}\left(\cos^4(\theta)+\sin^4(\theta)\right)}{C_{11}\ \sin^4(\theta)+C_{22}\ \cos^4(\theta)+\chi\ \sin^2(\theta)\cos^2(\theta)}. \qquad (5)$$

where $X=\left(\frac{C_{11}C_{22}-{C_{12}}^2}{C_{66}}-2C_{12}\right)$ and $Y=\left(C_{11}+C_{12}-\frac{C_{11}C_{12}-{C_{12}}^2}{C_{66}}\right)$. γ represents the in-plane orientation angle of the applied strain. The calculated values of Young's modulus and Poisson's ratio for the TaS_2/Sc_2CF_2 heterostructure, along with those for the individual TaS_2 and Sc_2CF_2 monolayers, are presented in Fig. 3(b and c). Notably, the heterostructure exhibits an enhanced Young's modulus compared to its constituent monolayers, indicating improved mechanical strength. The Young's modulus of the TaS_2/Sc_2CF_2 heterostructure is calculated to be 252.46 N m^{-1}, which is comparable to that of other van der Waals (vdW) heterostructures.[51–53] Meanwhile, its Poisson's ratio is obtained to be 0.31, remaining within a favorable range ($\nu < 0.5$), ensuring structural integrity under applied stress. Furthermore, since this value is larger than the conventional ductile–brittle threshold of 0.26,[54] the TaS_2/Sc_2CF_2 heterostructure can be classified as ductile. These characteristics make the TaS_2/Sc_2CF_2 heterostructure a promising candidate for applications requiring robust and flexible 2D materials.

To assess the thermal stability of the TaS_2/Sc_2CF_2 heterostructure, we conducted *ab initio* molecular dynamics (AIMD) simulations and phonon spectra, as depicted in Fig. 4(a and b). The temperature and total energy fluctuations were monitored throughout the simulation period to evaluate the robustness of the structure under thermal perturbations. The absence of significant structural distortions or energy divergence confirms the thermal stability of the heterostructure, indicating its potential viability for practical applications. In addition, the variations in total energy and temperature remain relatively small throughout the simulation, further affirming the structural integrity of the TaS_2/Sc_2CF_2 heterostructure under thermal perturbations, confirming the thermal stability. It is obvious from Fig. 4(b) that the absence of imaginary phonon modes throughout the Brillouin zone confirms the dynamical stability of the heterostructure. All these findings confirm the thermal and dynamical stability of the TaS_2/Sc_2CF_2 heterostructure at room temperature.

To examine charge redistribution at the TaS_2/Sc_2CF_2 interface, we calculate the planar-averaged charge density difference, as shown in Fig. 4(b). The charge density difference ($\Delta\rho$) is obtained by subtracting the charge densities of the isolated TaS_2 and Sc_2CF_2 monolayers from that of the combined heterostructure (ρ_H):

$$\Delta\rho=\rho_{\mathrm{H}}-(\rho_{\mathrm{TaS_2}}+\rho_{\mathrm{Sc_2CF_2}}). \qquad (6)$$

One can observe a notable charge redistribution near the contact region, indicating the presence of interlayer interactions facilitated by van der Waals (vdW) forces. Furthermore,

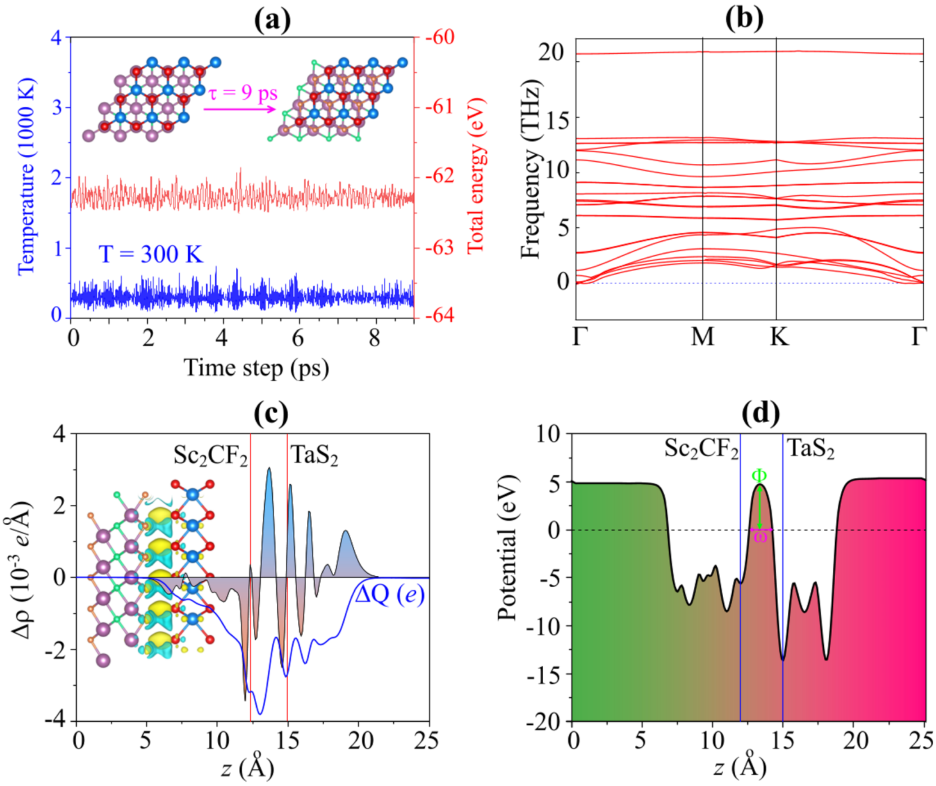

Fig. 4 (a) Temperature and total energy variations of the TaS_2/Sc_2CF_2 heterostructure obtained from AIMD simulations, (b) phonon spectra (c) planar-averaged charge density distribution and (d) electrostatic potential profile of the TaS_2/Sc_2CF_2 heterostructure. Charge accumulation and depletion regions are visualized in yellow and cyan, respectively.

positive charge accumulation occurs near the Sc_2CF_2 layer, while negative charge accumulation is observed near the TaS_2 layer. This signifies an interfacial charge transfer process, where electrons migrate from the Sc_2CF_2 layer to the TaS_2 layer. The movement of the electrons from the Sc_2CF_2 layer to the TaS_2 layer upon the formation of the TaS_2/Sc_2CF_2 heterostructure describes the formation of the p-type Schottky contact. The p-type doping of the Sc_2CF_2 monolayer made its Fermi level shift downwards, so that the band structure of the Sc_2CF_2 layer moved upwards relative to the Fermi level of the heterostructure. The calculated amount of transferred charge is approximately 4×10^{-3} electrons. Although the charge transfers between the TaS_2 and Sc_2CF_2 layers are small, the electrostatic potential of the TaS_2/Sc_2CF_2 heterostructure is plotted in Fig. 4(c) to analyze the charge distribution across the interface.

A notable charge redistribution is observed near the contact region, indicating the presence of interlayer interactions facilitated by vdW forces. Specifically, positive charge accumulation occurs near the Sc_2CF_2 layer, while negative charge accumulation is observed near the TaS_2 layer, signifying an interfacial charge transfer process where electrons migrate from the Sc_2CF_2 layer to the TaS_2 layer. This electron transfer upon heterostructure formation leads to the establishment of a p-type Schottky contact.

Consequently, the p-type doping effect in the Sc_2CF_2 monolayer results in a downward shift of its Fermi level, causing its band structure to move upwards relative to the Fermi level of the heterostructure. The amount of transferred charge is calculated to be approximately 4×10^{-3} electrons. Although the charge transfer between the TaS_2 and Sc_2CF_2 layers is relatively small, it induces the formation of an interface dipole, calculated to be 0.50 eV. This relatively small dipole facilitates charge carrier transport, significantly enhancing electron mobility across the heterostructure, which is highly beneficial for electronic applications. Furthermore, the electrostatic potential of the TaS_2/Sc_2CF_2 heterostructure, depicted in Fig. 4(c), provides deeper insights into charge distribution across the interface. The calculated work functions of TaS_2 and Sc_2CF_2 monolayers are 5.34 and 4.85 eV, which are in good agreement with previous reports.[55–57] The calculated work function of the TaS_2/Sc_2CF_2 heterostructure is intermediate between that of the constituent TaS_2 and Sc_2CF_2 monolayers. The work function of the TaS_2/Sc_2CF_2 heterostructure is found to be 5.02 eV, which is intermediate between those of its constituent layers, thereby confirming the direction of interfacial charge transfer. Additionally, through the electrostatic potential profiles, the tunneling barrier (Φ) and tunneling width (ω) can be obtained to be 4.75 eV and 1.28 Å, respectively, as depicted in Fig. 4(c). It is obvious that the efficiency of the carrier injection at the interface of the metal–semiconductor TaS_2/Sc_2CF_2 heterostructure can be evaluated *via* the comprehensive factor $C = \Phi \times \omega^2$, the tunneling probability T_P and the specific tunneling resistivity through the Simon model without bias voltage as follows:

$$T_P = \exp\left(-\frac{4\pi\omega\sqrt{2m_e\Phi}}{\hbar}\right), \quad \rho_t = \frac{2\hbar^2\omega}{3e^2\sqrt{2m_e\Phi}}T_P{}^{-1} \tag{7}$$

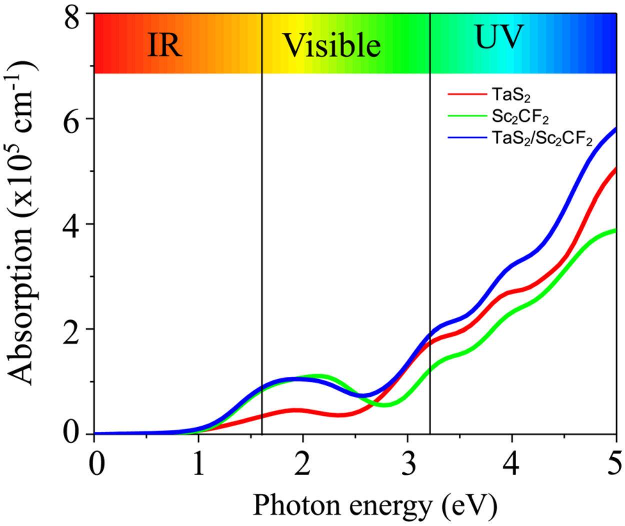

Fig. 5 Optical absorption of the TaS_2/Sc_2CF_2 heterostructure for the TS2 stacking configuration.

The obtained C, T_P and ρ_t of the TaS_2/Sc_2CF_2 heterostructure are to be 7.42 eV.Å2, 6.38% and 1.62×10^{-10} Ω cm^2, respectively. Notably, a lower C value corresponds to a higher tunneling probability T_P, leading to enhanced carrier injection efficiency. Moreover, the low ρ_t value implies that the charge carriers experience minimal obstruction at the interface, supporting efficient carrier injection. This feature is particularly advantageous for the design of high-performance electronic and optoelectronic devices such as transistors and photodetectors. To further explore the optical response, we calculated the absorption spectrum of the $TaS_2/Sc_2CF_2Sc_2CF_2$ heterostructure, as shown in Fig. 5. It is evident that the integration of TaS_2 and Sc_2CF_2 layers leads to a significant enhancement in the absorption coefficient compared with the individual monolayers. Remarkably, the absorption coefficient of the heterostructure reaches up to 6×10^5 cm^{-1}, underscoring its strong potential for optoelectronic applications.

Furthermore, the tunability of the TaS_2/Sc_2CF_2 heterostructure plays a crucial role in optimizing its electronic properties for various applications. Therefore, it is essential to examine how the electronic properties and contact behavior of the TaS_2/Sc_2CF_2 heterostructure respond to an applied electric field. The external electric field was applied perpendicular to the TaS_2/Sc_2CF_2 heterostructure by introducing a sawtooth-like potential. Specifically, the field was oriented along the z axis, directed from the TaS_2 layer toward the Sc_2CF_2 layer, as illustrated in Fig. 6(a). It is observed that the electric field induces a transition from Schottky to ohmic contact, as well as a conversion from n-type to p-type Schottky contact, as depicted in Fig. 6(b). For instance, under the application of a positive electric field, the electron barrier Φ_e increases, while the hole barrier Φ_h decreases correspondingly. This indicates that the TaS_2/Sc_2CF_2 heterostructure retains its p-type Schottky contact with a reduced hole barrier Φ_h, facilitating enhanced hole injection at the interface. A lower Φ_h means that the hole injection into the Sc_2CF_2 layer is easier, which can significantly

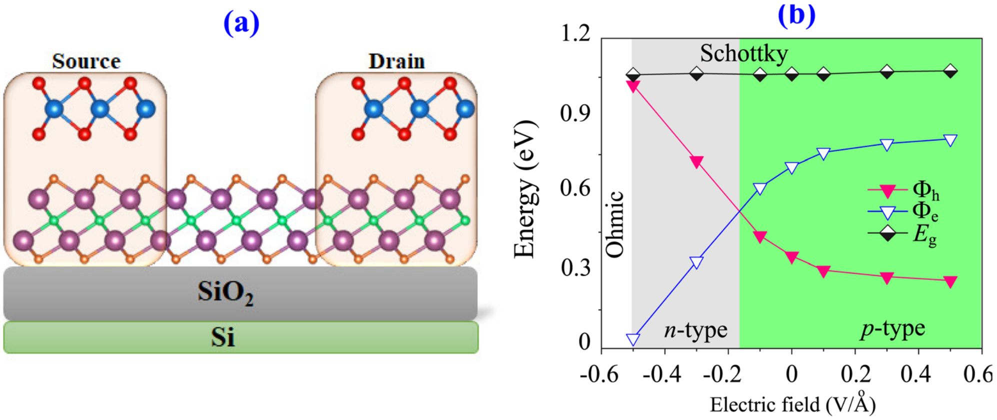

Fig. 6 (a) Schematic illustration of the electric field and (b) the tunability of the Schottky barriers and Schottky contact under applied electric fields.

improve device performance in applications such as transistors and optoelectronic components, as illustrated in Fig. 6(a). Conversely, under the application of a negative electric field, the electron barrier Φ_e is narrowed, while the hole barrier Φ_h is widened correspondingly. As illustrated in Fig. 6(b), when the negative electric field strength drops below -0.2 V Å^{-1}, Φ_e becomes narrower than Φ_h, indicating a transition from a p-type to an n-type Schottky contact. More interestingly, as the negative electric field further decreases beyond -0.5 V Å^{-1}, the electron barrier Φ_e continues to narrow and eventually approaches zero. This signifies a barrier-free charge injection process, facilitating highly efficient electron transport across the heterostructure. This finding indicates a transition toward ohmic contact, where charge carriers can move freely without significant resistance at the interface.

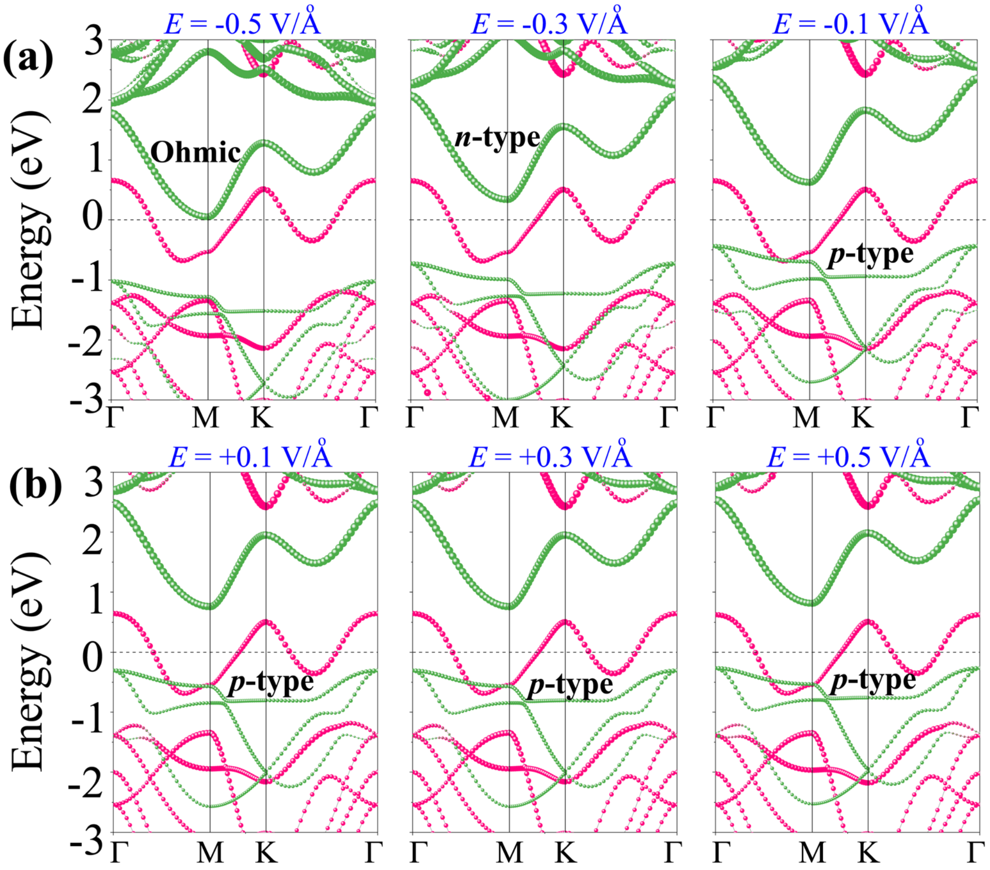

Fig. 7 (a) Schematic illustration of the electric field and (b) the tunability of the Schottky barriers and Schottky contact under applied electric fields.

To better understand the physical mechanism underlying the tunability of the TaS_2/Sc_2CF_2 heterostructure, we analyze its projected band structures under varying electric fields, as shown in Fig. 7. As illustrated in Fig. 7(a), the application of a negative electric field induces a downward shift in the band edges of the semiconductor Sc_2CF_2 layer toward the Fermi level, effectively reducing the barrier for electron injection. When the negative electric field strength drops below -0.2 V $Å^{-1}$, the CB of the Sc_2CF_2 layer moves closer to the Fermi level than the VB, signifying the transition from a p-type to an n-type Schottky contact. At a negative electric field strength below -0.5 V $Å^{-1}$, the CB of the Sc_2CF_2 layer crosses the Fermi level, confirming the transition from Schottky to ohmic contact. It is evident that the electric field strongly influences the Sc atoms and the orbital hybridization between C and F atoms, while its effect on the Ta and S atoms is comparatively weak, as illustrated in Fig. S5. This indicates that the energy barrier for electron injection is effectively eliminated, allowing charge carriers to flow freely across the interface without resistance. Fig. 7(b) illustrates the projected band structures of the TaS_2/Sc_2CF_2 heterostructure under the influence of a positive electric field. The band edges of the Sc_2CF_2 layer exhibit an upward shift, moving away from the Fermi level. This shift increases the Schottky barrier height for electron injection while reducing the barrier for hole transport, reinforcing the p-type Schottky contact. Furthermore, it should be noted that the amount of transferred charge increases under negative fields, favoring electron injection and ohmic transition, whereas it decreases under positive fields, stabilizing hole-dominated p-type contact. All these findings suggest that the electric fields induce significant modifications in the charge injection mechanism and contact behavior of the TaS_2/Sc_2CF_2 heterostructure, making it a highly tunable system for electronic applications.

4 Conclusions

In summary, we employed first-principles calculations to design and investigate the electronic properties and contact performance tunability of the TaS_2/Sc_2CF_2 heterostructure under applying electric fields. Our results demonstrate that the TaS_2/Sc_2CF_2 heterostructure is both energetically favorable and thermally stable, suggesting that it could be synthesized experimentally. The heterostructure is primarily governed by weak vdW interactions, ensuring the preservation of intrinsic properties of its constituent monolayers. Furthermore, the integration of TaS_2 with Sc_2CF_2 enhances the elastic constants and Young modulus, improving mechanical rigidity. More importantly, the TaS_2/Sc_2CF_2 heterostructure forms a Schottky contact with a low Schottky barrier of 0.36 eV, which can be actively tuned *via* an applied electric field. Under a negative electric field, the system undergoes a transition from Schottky to ohmic contact, alongside a conversion from n-type to p-type Schottky contact. This tunability facilitates barrier-free charge injection, positioning the TaS_2/Sc_2CF_2 heterostructure as a promising candidate for next-generation electronic and optoelectronic applications, such as transistors and photodetectors.

Conflicts of interest

There are no conflicts to declare.

Data availability

The data that support the findings of this study are available from the corresponding author upon reasonable request.

Supplementary information is available. See DOI: **https://doi.org/10.1039/d5ra05385d**.

References

1 J. Zhao, D. Ma, C. Wang, Z. Guo, B. Zhang, J. Li, G. Nie, N. Xie and H. Zhang, *Nano Res.*, 2021, **14**, 897–919.
2 Z. Cheng, R. Cao, K. Wei, Y. Yao, X. Liu, J. Kang, J. Dong, Z. Shi, H. Zhang and X. Zhang, *Adv. Sci.*, 2021, **8**, 2003834.
3 K. S. Novoselov, A. K. Geim, S. V. Morozov, D.-e. Jiang, Y. Zhang, S. V. Dubonos, I. V. Grigorieva and A. A. Firsov, *Science*, 2004, **306**, 666–669.
4 L. Liu, Y. Feng and Z. Shen, *Phys. Rev. B:Condens. Matter Mater. Phys.*, 2003, **68**, 104102.
5 G. Giovannetti, P. A. Khomyakov, G. Brocks, P. J. Kelly and J. Van Den Brink, *Phys. Rev. B:Condens. Matter Mater. Phys.*, 2007, **76**, 073103.
6 C. R. Dean, A. F. Young, I. Meric, C. Lee, L. Wang, S. Sorgenfrei, K. Watanabe, T. Taniguchi, P. Kim, K. L. Shepard, et al., *Nat. Nanotechnol.*, 2010, **5**, 722–726.
7 S. Manzeli, D. Ovchinnikov, D. Pasquier, O. V. Yazyev and A. Kis, *Nat. Rev. Mater.*, 2017, **2**, 1–15.
8 S.-H. Su, Y.-T. Hsu, Y.-H. Chang, M.-H. Chiu, C.-L. Hsu, W.-T. Hsu, W.-H. Chang, J.-H. He, L.-J. Li, et al., *Small*, 2014, **10**, 2589–2594.
9 M. Kang, B. Kim, S. H. Ryu, S. W. Jung, J. Kim, L. Moreschini, C. Jozwiak, E. Rotenberg, A. Bostwick and K. S. Kim, *Nano Lett.*, 2017, **17**, 1610–1615.
10 Z. Yu, Z.-Y. Ong, S. Li, J.-B. Xu, G. Zhang, Y.-W. Zhang, Y. Shi and X. Wang, *Adv. Funct. Mater.*, 2017, **27**, 1604093.
11 Q. Zeng and Z. Liu, *Adv. Electron. Mater.*, 2018, **4**, 1700335.
12 S. Das, A. Prakash, R. Salazar and J. Appenzeller, *ACS Nano*, 2014, **8**, 1681–1689.
13 J. Chen, M.-Y. Sun, Z.-H. Wang, Z. Zhang, K. Zhang, S. Wang, Y. Zhang, X. Wu, T.-L. Ren, H. Liu, et al., *Nano-Micro Lett.*, 2024, **16**, 264.
14 Y. Gogotsi, *Chem. Mater.*, 2023, **35**(21), 8767–8770.
15 B.-F. Guo, Y.-J. Wang, C.-F. Cao, Z.-H. Qu, J. Song, S.-N. Li, J.-F. Gao, P. Song, G.-D. Zhang, Y.-Q. Shi, et al., *Adv. Sci.*, 2024, **11**, 2309392.
16 S. Wan, Y. Chen, C. Huang, Z. Huang, C. Liang, X. Deng and Q. Cheng, *Nature*, 2024, **634**, 1103–1110.
17 X. Li, Z. Huang, C. E. Shuck, G. Liang, Y. Gogotsi and C. Zhi, *Nat. Rev. Chem.*, 2022, **6**, 389–404.
18 Q. Zhong, Y. Li and G. Zhang, *Chem. Eng. J.*, 2021, **409**, 128099.
19 Y. Shin, J. Kwon, Y. Jeong, K. Watanabe, T. Taniguchi, S. Im and G.-H. Lee, *Small*, 2022, **18**, 2200882.

20 X. Zhou, X. Hu, J. Yu, S. Liu, Z. Shu, Q. Zhang, H. Li, Y. Ma, H. Xu and T. Zhai, *Adv. Funct. Mater.*, 2018, **28**, 1706587.

21 N. F. Hinsche and K. S. Thygesen, *2D Materials*, 2017, **5**, 015009.

22 X.-L. Yu, D.-Y. Liu, Y.-M. Quan, J. Wu, H.-Q. Lin, K. Chang and L.-J. Zou, *Phys. Rev. B*, 2017, **96**, 125138.

23 Q. Tian, C. Ding, X. Qiu, Q. Meng, K. Wang, F. Yu, Y. Mu, C. Wang, J. Sun and Y. Zhang, *Sci. China:Phys., Mech. Astron.*, 2024, **67**, 256811.

24 A. Hassan, M. A. Nazir, Y. Shen, Y. Guo, W. Kang and Q. Wang, *ACS Appl. Mater. Interfaces*, 2021, **14**, 2177–2184.

25 C. G. Ayani, M. Bosnar, F. Calleja, A. P. Solé, O. Stetsovych, I. M. Ibarburu, C. Rebanal, M. Garnica, R. Miranda, M. M. Otrokov, et al., *Nano Lett.*, 2024, **24**, 10805–10812.

26 X. Xue, X. Wang and W. Mi, *Appl. Surf. Sci.*, 2018, **455**, 963–969.

27 M. Malaki, X. Jiang, H. Wang, R. Podila, H. Zhang, P. Samorì and R. S. Varma, *Chem. Eng. J.*, 2023, **463**, 142351.

28 M. Khazaei, A. Ranjbar, M. Arai, T. Sasaki and S. Yunoki, *J. Mater. Chem. C*, 2017, **5**, 2488–2503.

29 S. Ghosh, M. Akhtaruzzaman and M. Uddin, *Mater. Today Commun.*, 2025, 113524.

30 L. Zhang, Z. Yang, T. Gong, R. Pan, H. Wang, Z. Guo, H. Zhang and X. Fu, *J. Mater. Chem. A*, 2020, **8**, 8813–8830.

31 Y. Zhang, B. Sa, N. Miao, J. Zhou and Z. Sun, *J. Mater. Chem. A*, 2021, **9**, 10882–10892.

32 E. Balcı, Ü. Ö. Akkuş and S. Berber, *J. Mater. Chem. C*, 2017, **5**, 5956–5961.

33 X.-H. Cui, X.-H. Li, R.-Z. Zhang, H.-L. Cui and H.-T. Yan, *Surf. Interfaces*, 2022, **33**, 102193.

34 R.-Z. Zhang, X.-H. Cui, H.-L. Cui and X.-H. Li, *Appl. Surf. Sci.*, 2022, **581**, 152360.

35 Z. Cui, G. Zhang, S. Zhang and L. Wang, *Micro Nanostruct.*, 2024, **193**, 207922.

36 S.-T. Nguyen, C. Q. Nguyen, N. N. Hieu, H. V. Phuc and C. V. Nguyen, *Langmuir*, 2023, **39**, 17251–17260.

37 J. Bao, B. Zhu, F. Zhang, X. Chen, H. Guo, J. Qiu, X. Liu and J. Yu, *Int. J. Hydrogen Energy*, 2021, **46**, 39830–39843.

38 J. Zhang, Y. Deng, H. Liu, R. Zhou, G. Hao and R. Zhang, *J. Phys. Chem. Solids*, 2024, **185**, 111757.

39 G. Kresse and J. Furthmüller, *Phys. Rev. B:Condens. Matter Mater. Phys.*, 1996, **54**, 11169–11186.

40 J. P. Perdew, K. Burke and M. Ernzerhof, *Phys. Rev. Lett.*, 1996, **77**, 3865–3868.

41 S. Grimme, J. Antony, S. Ehrlich and H. Krieg, *J. Chem. Phys.*, 2010, **132**, 154104.

42 H. J. Monkhorst and J. D. Pack, *Phys. Rev. B*, 1976, **13**, 5188–5192.

43 R. Car and M. Parrinello, *Phys. Rev. Lett.*, 1985, **55**, 2471.

44 W. G. Hoover, *Phys. Rev. A*, 1985, **31**, 1695.

45 S. Baroni, S. De Gironcoli, A. Dal Corso and P. Giannozzi, *Rev. Mod. Phys.*, 2001, **73**, 515.

46 N. D. Khang, C. Q. Nguyen, L. M. Duc and C. V. Nguyen, *Nanoscale Adv.*, 2023, **5**, 2583–2589.

47 Q. Wang, L. Cao, S.-J. Liang, W. Wu, G. Wang, C. H. Lee, W. L. Ong, H. Y. Yang, L. K. Ang, S. A. Yang, et al., *npj 2D Mater. Appl.*, 2021, **5**, 71.

48 X. Gao, Y. Shen, Y. Ma, S. Wu and Z. Zhou, *Carbon*, 2019, **146**, 337–347.

49 V. Wang, N. Xu, J.-C. Liu, G. Tang and W.-T. Geng, *Comput. Phys. Commun.*, 2021, **267**, 108033.

50 N. T. Hung, A. R. Nugraha and R. Saito, *J. Phys. D: Appl. Phys.*, 2018, **51**, 075306.

51 C. Mahala, M. D. Sharma and M. Basu, *New J. Chem.*, 2019, **43**, 7001–7010.

52 S. Ahmad, K. Sohail, L. Chen, H. Xu, H. Din and Z. Zhou, *Int. J. Hydrogen Energy*, 2023, **48**, 25354–25365.

53 H. Meng, Z. Cui, P. Wu, S. Zhang and L. Wang, *Mater. Today Commun.*, 2025, 112830.

54 R. M. Christensen, *Proc. R. Soc. A*, 2020, **476**, 20190719.

55 J. Ravnik, Y. Vaskivskyi, J. Vodeb, P. Aupič, I. Vaskivskyi, D. Golež, Y. Gerasimenko, V. Kabanov and D. Mihailovic, *Nat. Commun.*, 2021, **12**, 3793.

56 J. Ye, X. Wang, D. Yu, S. Yu, F. Ai, S. Lu, Q. Xiao, J. Huang and Q. Xie, *Int. J. Hydrogen Energy*, 2025, **148**, 150039.

57 Y. Tang, M. Liu, X. Zhong, K. Qiu, L. Bai, B. Ma, J. Wang and Y. Chen, *Results Phys.*, 2024, **60**, 107706.